

Snapshot light-field laryngoscope

Shuaishuai Zhu,^{a,b} Peng Jin,^{b,*} Rongguang Liang,^c Liang Gao^{a,d,*}

^a University of Illinois at Urbana-Champaign, Department of Electrical and Computer Engineering, 306 N. Wright St., Urbana, USA, 61801

^b Harbin Institute of Technology, Center of Ultra-precision Optoelectronic Instrument, 2 Yikuang St., Harbin, China, 150080

^c University of Arizona, College of Optical Sciences, Tucson, USA, 85721

^d University of Illinois at Urbana-Champaign, Beckman Institute for Advanced Science and Technology, 405 N. Mathews Ave., Urbana, USA, 61801,

Abstract. The convergence of recent advances in optical fabrication and digital processing yields a new generation of imaging technology—light-field cameras, which bridge the realms of applied mathematics, optics, and high-performance computing. Herein for the first time, we introduce the paradigm of light-field imaging into laryngoscopy. The resultant probe can image the three-dimensional (3D) shape of vocal folds within a single camera exposure. Furthermore, to improve the spatial resolution, we developed an image fusion algorithm, providing a simple solution to a long-standing problem in light-field imaging.

Keywords: Three-dimensional image acquisition, Computational imaging, Medical optics instrumentation.

*Fourth Author, E-mail: gaol@illinois.edu; *Second Author, E-mail: p.jin@hit.edu.cn

1 Introduction

Currently, approximately 7.5 million people in the United States suffer from voice disorders due to either trauma or diseases. Human vocal fold vibration is a complex three-dimensional (3D) movement. An unusual 3D shape of the vocal fold is a hallmark of a variety of vocal diseases, such as polyps, nodules, recurrent nerve paralysis, and cancer^{1,2}. The acquisition of 3D data can facilitate the theoretical modeling of vocal fold dynamics, providing insights into vocal fold pathology^{3,4} and fundamental phonation research^{5,6}.

The standard in-office methods for diagnosing voice disorders include videostroboscopy⁷ and high-speed videoendoscopy⁸. Both techniques image only the horizontal movement of vocal folds. They cannot measure the movement of vocal folds along the air flow direction. Despite its vital importance, 3D laryngeal imaging is currently only available via a few methods—namely, computed tomography (CT)^{3,9}, magnetic resonant imaging (MRI)^{10,11}, laser triangulation^{12,13}, and

optical coherence tomography (OCT)^{14,15}. Although CT, MRI, and OCT can measure the full 3D profile of vocal cords, the prolonged acquisition time restricts their use in dynamic imaging. In addition, CT and MRI are costly, and they require special operating rooms. Alternatively, laser triangulation features a high acquisition speed. Nonetheless, it measures depths at only selected points or lines, resulting in a limited field of view. The lack of an en face image jeopardizes the sensitivity and specificity of diagnosis.

To enable fast imaging of vocal folds in 3D, for the first time, we introduce the paradigm of light-field imaging¹⁶ into laryngoscopy. The resultant system, which we term a light-field laryngoscope (LFL), can capture a volumetric image of vocal folds within a single snapshot. Rather than acquiring only two-dimensional (x, y) (x, y , spatial coordinates) images, light-field cameras acquire both the spatial and angular information of remittance. The resultant four-dimensional (4D) (x, y, θ, ϕ) (θ, ϕ , 2D light emitting angles) datacube can be mathematically converted into a 3D (x, y, z) (z , depth) image through postprocessing¹⁷. Since no scanning is required, the 3D frame rate is limited by only the camera's data readout bandwidth. Although the light-field imaging was first proposed by Lippmann¹⁸ in 1908, not until the last decade were breakthroughs achieved in demonstrating its biomedical applications. For example, Noah et al. developed a light-field otoscope for 3D imaging of the tympanic membrane in vivo¹⁹. Amir et al. constructed a light-field endoscope using a hexagonal liquid crystal lens array²⁰. Massino et al. showed the potential of light-field cameras in retinal imaging²¹. Lastly, using a light-field microscope, Robert et al. recorded neuronal activity in 3D with an unprecedented frame rate²².

2 Light-field laryngoscope design

We show the optical schematic and a photograph of the distal end of LFL probe in Fig. 1(a) and 1(b), respectively. The illumination light is guided to the tip of the probe through a multimode

glass fiber (Thorlabs M28L01) and reflected towards the object by a right-angle prism (Edmund 84-506). The back-reflected light is collected by an objective lens (Edmund 49-657, $f = 18$ mm), forming an intermediate image S_1 at the distal end of a gradient-index (GRIN) lens (Gradient Lens Corporation COAT14-45-219; length, 219 mm (one pitch)). This intermediate image is then relayed by the GRIN lens to its proximal end, followed by being magnified by an optical system which consists of a microscope objective (Nikon CF Plan, $f = 40$ mm, $NA = 0.13$) and a tube lens (Thorlabs AC254-100-A, $f = 100$ mm). The magnified image is directed towards two imaging channels by a beamsplitter. While the transmitted image is directly measured by a high-resolution detector array (Point Grey CR-POE-20S2C-CS), the reflected image is acquired by a custom light-field camera which comprises a microlens array (MLA) (Advanced Microoptic Systems GmbH APO-Q-P148-R0.73, $f = 1.6$ mm) and a detector array (Point Grey BFLY-PGE-20E4M-CS). Herein we adopt a 2.0 light-field camera configuration—the distance between the MLA and the detector array is smaller than the focal length of the MLA¹⁶. We summarize the imaging parameters of two channels above (high-resolution (HR) and light-field (LF)) in Table 1. The geometrical dimensions of our prototype probe are similar to those of commercial laryngoscopes, with a nominal working distance of 65 mm and an outside diameter around 10 mm.

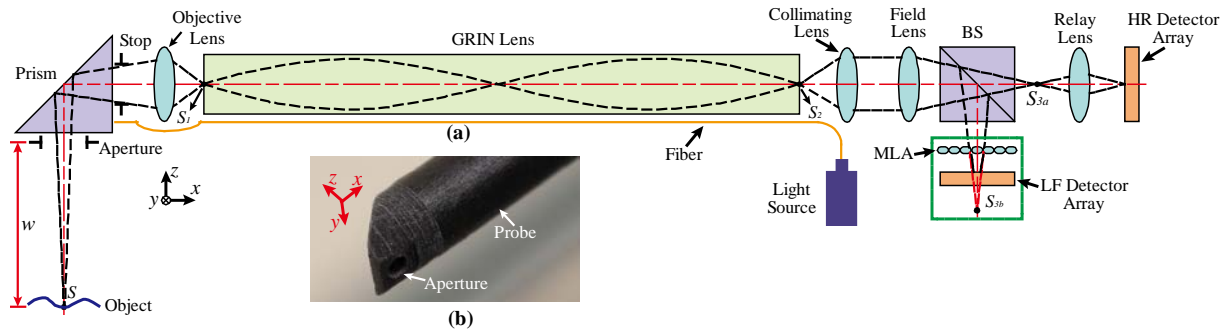


Fig. 1 Schematic of a light-field laryngoscope. (a) Optical setup. The detector arrays in the HR and LF channel are referred to as HR and LF detector array, respectively. (b) Photograph of the distal end of the probe. GRIN, Graded-index; BS, Beam Splitter; MLA, Microlens Array; HR, High-Resolution; LF, Light-field.

Table 1 Specifications of two channels.

	Spatial Resolution (pixels)	Depth Precision	Depth Range
High-resolution channel	1920×1080	Not applicable	Not applicable
Light-field channel	640×360	0.37 mm	62.5 mm – 67.5 mm

Figure 2 shows the image processing pipeline, which consists of four steps, namely I) resolution enhancement, II) disparity estimation, III) depth reconstruction, and IV) combination of depth map and HR image. In Step I, we first derive the resolution ratio between the HR image and a single elemental image by imaging a calibration object (a chess board). Then we super-resolve each elemental image in the LF image using the HR image as the reference by a patch-based image super-resolution algorithm²³. We downsample the HR image by a factor of the resolution ratio, followed by extracting a series of image patch pairs $\{h_i, l_i\}_{i=1}^n$. Here h_i and l_i denote the image patches extracted from the original and the downsampled HR images, respectively, and i is the index enumerating the image patches. We save these image patches in dictionary D_{ref} . For each patch p_j (5×5 pixels) in an elemental image, we search in D_{ref} and identify nine patches $\{l'_k\}_{k=1}^9$ which have the smallest distances in the L_2 norm from p_j . We estimate the high-resolution representation \hat{h}_j of p_j by

$$\hat{h}_j = \frac{\sum_{k=1}^9 w_k h'_k}{\sum_{k=1}^9 w_k}, \quad (1)$$

where $w_k = \exp \frac{-\|p_j - l'_k\|^2}{2\sigma^2}$. Here σ^2 is a hyper-parameter, and we determine its value by using the Stanford light-field database²⁴ as a cross validation dataset.

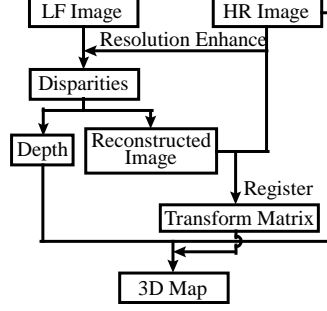


Fig. 2 Flowchart of the image processing pipeline.

In step II, we consider the MLA as an array of stereo cameras and derive disparities from the correspondent elemental images pairwise. We illustrate the underlying principle using a simplified one-dimensional example (Fig. 3). The purple dashed lines denote the chief rays associated with microlenses. The extensions of these light rays (red dashed lines) converge to a virtual image point S_{3b} . Figure 3(b) shows the elemental images M_1 , M_2 , and M_3 formed behind the correspondent microlenses. For each elemental image pair, we identify the matched features by a searching algorithm based on correlation distance²⁵. In brief, we first extract feature sets $\{f_{i,1}\}_{i=1}^{m_1}$ and $\{f_{i,2}\}_{i=1}^{m_2}$ from two elemental images, respectively. For each feature $f_{i,1}$, we search the correspondent neighborhood in $\{f_{i,2}\}_{i=1}^{m_2}$ and identify $f'_{j,2}$ which has the smallest correlation distance to $f_{i,1}$. We term $f'_{j,2}$ as the matched feature of $f_{i,1}$. Next, we calculate the disparity, D , as the relative distance between these two matched image features (Fig. 3(b)).

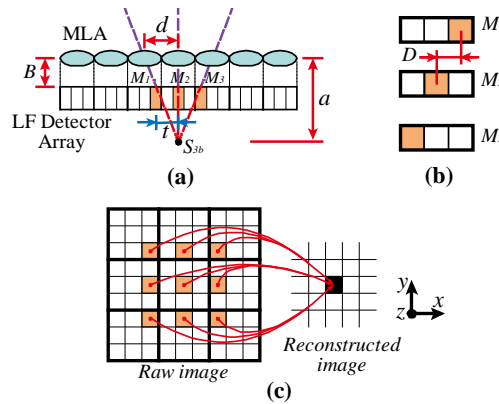


Fig. 3 Light-field reconstruction. (a) Image formation in one dimension. (b) Zoomed-in view of elemental images M_1 , M_2 , and M_3 . The disparity D is calculated as the relative distance between two matched image pixels. (c) Two-dimensional image reconstruction.

In Step III, we derive depths through disparities. As shown in Fig. 3(a), in the global coordinate, we use t to denote the absolute distance between the two matched pixels in M_1 and M_2 . Then the disparity can be calculated by $D = d - t$, where d is the MLA pitch. Using trigonometric relations, we get

$$(a - B)/a = t/d, \quad (2)$$

where B is the distance from the MLA to the LF detector array, and a is the distance from the MLA to the virtual image S_{3b} . Substituting d with $d = D + t$ yields

$$a = B \times d/D. \quad (3)$$

To calculate the object depth, w , we project the virtual image S_{3b} back to the object space. The relation between w and a can be experimentally determined through calibration²⁶.

In Fig. 3(c), we further generalize the scheme above to the two-dimensional case. In each elemental image, the orange pixel collects the light rays converging to the same virtual intermediate image point, S_{3b} . We group these pixels and map their values to a single pixel in the intermediate image. Following this procedure pixelwise yields a reconstructed image²⁵.

In light-field imaging, there is a trade-off between the spatial and angular resolution because the total number of 4D light-field datacube voxels cannot exceed the total number of sensor pixels. To some extent, this trade-off can be mitigated by employing compressed sensing algorithms²⁷⁻²⁹. However, these techniques are computationally extensive, and they highly rely on the ill-posed assumption that the light-field is sparse in a given domain. Also, the requirement of multiple camera exposures^{27,28} makes them unsuitable for imaging dynamic scenes. By contrast, in the

proposed LFL, we alleviate this problem through fusing the depth map with a high-resolution reference image in Step IV. We warp the depth map to the actual size of HR image through a transform matrix derived by registering the reconstructed image from the LF channel and the HR image. Then we mathematically combine the warped depth map and the HR image to generate a high-resolution 3D representation of the original scene.

3 Experiments

The depth precision in the LFL is determined by a myriad of factors, namely pitch size of MLA, the distance from the MLA to the sensor, the pixel size the sensor, NA and the vignetting³⁰. To evaluate the depth precision in our prototype, we scanned a point source along both the x - and z -axes. Twelve steps were taken along the x -axis with step size set as 0.8 mm, while nine steps were taken along the z -axis with step size set as 0.64 mm. The mean and standard deviation of the measured depths along the x -axis at each z -axis step are shown in Fig. 4. The black dashed line shows the ground truth. The root mean square error (RMSE) of the average measured depth along the x -axis is 0.07 mm. The depth precision is estimated as the average standard deviation along the z -axis. The result approximates 0.37 mm, providing an effective depth-to-resolution greater than ten.

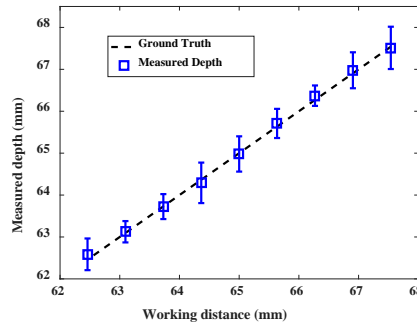


Fig. 4 Quantification of depth precision in light-field laryngoscope.

To assess the lateral resolution, we imaged a 1951 USAF resolution test target at the nominal working distance (65 mm) of the LFL. Figure 5(a) shows the reconstructed image of the test target with a zoomed-in inset view of bars in Group 4 and 5. In Fig. 5(b), we plot the intensity profile along a green dashed line in Fig. 5(a) (inset). The Lord Rayleigh’s criterion states that two overlapping slit images are resolvable when the irradiance of the saddle point between two fringes is lower than $8/\pi^2$ times of the maximum irradiance³¹. Based on this criterion, the bars of group 4 element 4, as shown in the orange dashed rectangle, are the finest resolvable features. Therefore, the lateral resolution of the LFL is 22.6 lp/mm.

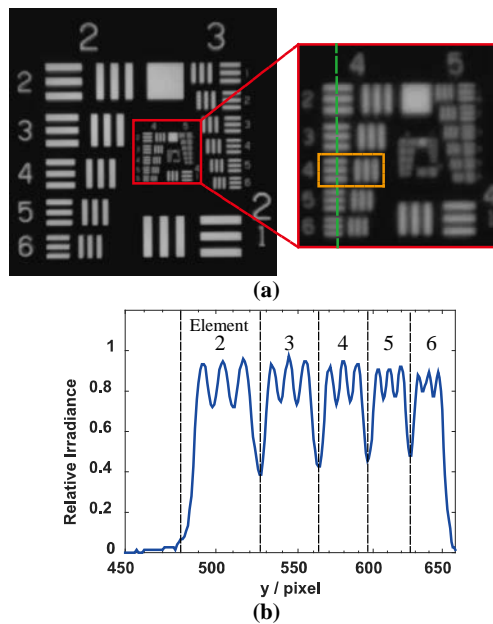


Fig. 5 Spatial resolution of the light-field laryngoscope. (a) Reconstructed in-focus image of a 1951 USAF resolution target. (b) Intensity profile along the green dashed line in Fig. 5(a) inset.

Next, we compare this value to the diffraction limit, which is calculated as $R_d = 1/2r = NA/1.22\lambda$, where r is the radius of airy disk, λ is the wavelength of the incident light, and NA is the numerical aperture. Given $\lambda = 0.6 \mu\text{m}$ and $NA = 0.02$, we have $R_d = 27.3 \text{ lp/mm}$, which is greater than the experimental resolution of the LFL. We attribute this discrepancy to two reasons. First, we constructed the LFL prototype using only off-the-shelf lenses. The cumulative geometric

aberrations blur the image. Second, the employment of a GRIN lens introduces a considerable level of chromatic aberration³², which also degrades the imaging performance. Although beyond the scope of this paper, we can potentially overcome these problems by replacing these off-the-shelf lenses and GRIN lens with custom ones.

Finally, to demonstrate the 3D imaging capability of the LFL, we performed two phantom experiments. First, we used a tilted paper surface with letters as an object. A reference photograph is shown in Fig. 6(a). Captured by a single snapshot, the reconstructed 3D image is shown in Fig. 6(b). The recovered surface tilt angle matches with the experimental setup. Next, we imaged a vocal fold phantom (Fig. 6(c)), using “vessels” and “vocal fold edges” as features for disparity estimation. Because LFL measures depths only at distinct feature points, we filled the blank areas using interpolation on the assumption that the phantom surface is naturally continuous in slope and curvature. Figure 6(d) shows the reconstructed 3D image, agreeing well with the ground truth.

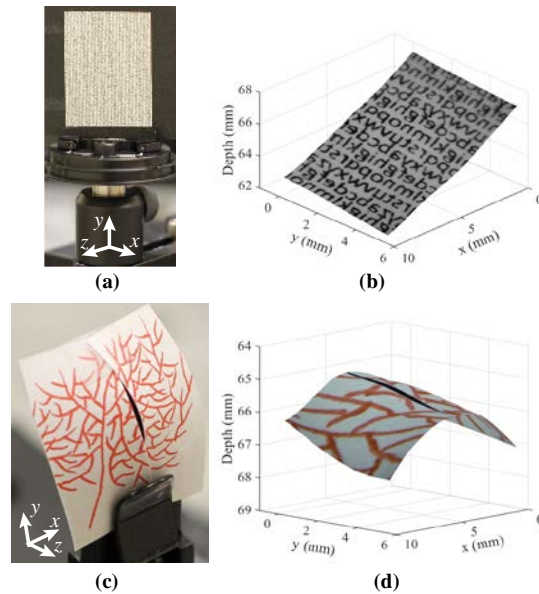


Fig. 6 3D phantom imaging. (a) Reference photograph of a tilted paper surface with letters. (b) Reconstructed 3D image. (c) Reference photograph of a vocal fold phantom. (d) Reconstructed 3D image.

The overall layout of LFL is simple, and it can be built using only off-the-shelf optical components. The projected manufacturing cost is comparable to the conventional medical laryngoscopes that are routinely used in the primary care clinics. Also, thanks to its simplicity, the system requires rudimentary training to operate.

4 Conclusions

In summary, we constructed a 3D imaging LFL. Rather than measuring only the spatial information, the LFL acquires the spatial and angular information of the incident light rays in parallel. Such a measurement leads to a recovery of a 3D representation of the original scene with high fidelity. Due to a snapshot acquisition format, the 3D imaging speed is limited by only the camera's readout speed, which can be potentially up to 1,000 volumes/sec when coupled to a high-speed camera³³. In light of its unprecedented 3D imaging performance, we anticipate that LFL will open a new area of investigation in both the clinical diagnostics and fundamental phonation research.

Acknowledgments

This work was supported in part by NSF CAREER grant (1652150) and discretionary funds from UIUC. We thank Kuida Liu for his contribution to the super-resolution algorithm just as James Hutchinson for the close reading of the manuscript. We also gratefully acknowledge the financial support from the China Scholarship Council.

References

1. J. W. Dankbaar and F. A. Pameijer, "Vocal cord paralysis: anatomy, imaging and pathology," *Insights into Imaging* **5**(6), 743-751 (2014) [doi: 10.1007/s13244-014-0364-y].

2. F. G. Dikkers and P. G. Nikkels, "Benign lesions of the vocal folds: histopathology and phonotrauma," *Ann. Oto. Rhinol. Laryn.* **104**(1), 698-703 (1995) [doi: [10.1177/000348949510400905](https://doi.org/10.1177/000348949510400905)].
3. H. Bakhshaei, C. Moro, K. Kost, and L. Mongeau, "Three-dimensional reconstruction of human vocal folds and standard laryngeal cartilages using computed tomography scan data," *J. Voice* **27**(6), 769-777 (2013) [doi: [10.1016/j.jvoice.2013.06.003](https://doi.org/10.1016/j.jvoice.2013.06.003)].
4. T. Sanuki, "Endoscopic mode for three-dimensional CT display of normal and pathologic laryngeal structures," *Otolaryng. Head Neck (Tokyo)* **69**(3), 211-216 (1997).
5. L. Cveticanin, "Review on mathematical and mechanical models of the vocal cord," *J. Appl. Math.* **2012**(5), 928591 (2012) [doi: 10.1155/2012/928591].
6. Q. Xue, X. Zheng, R. Mittal, and S. Bielaowicz, "Subject-specific computational modeling of human phonation," *J. Acoust. Soc. Am.* **135**(3), 1445-1456 (2014) [doi: 10.1121/1.4864479].
7. D. D. Mehta and R. E. Hillman, "Current role of stroboscopy in laryngeal imaging," *Curr. Opin. Otolaryngol. Head Neck Surg.* **20**(6), 429-436 (2012) [doi: [10.1097/MOO.0b013e3283585f04](https://doi.org/10.1097/MOO.0b013e3283585f04)].
8. D. D. Deliyiski, P. P. Petrushev, H. S. Bonilha, T. T. Gerlach, B. Martin-Harris, and R. E. Hillman, "Clinical implementation of laryngeal high-speed videoendoscopy: challenges and evolution," *Folia Phoniatr. Logop.* **60**(1), 33-44 (2007) [doi: [10.1159/000111802](https://doi.org/10.1159/000111802)].
9. E. Yumoto, T. Sanuki, M. Hyodo, Y. Yasuhara, and T. Ochi, "Three-Dimensional Endoscopic Mode for Observation of Laryngeal Structures by Helical Computed Tomography," *Laryngoscope* **107**(11), 1530-1537 (1997) [doi: 10.1097/00005537-199711000-00020].
10. T. Frauenrath, W. Renz, J. Rieger, A. Goemmel, C. Butenweg, and T. Niendorf, "High spatial resolution 3D MRI of the Larynx using a dedicated TX/RX phased array coil at 7.0T," *Proceedings of International Society for Magnetic Resonance in Medicine*, D. K. Sodickson, Ed., p. 894, Stockholm, Sweden (2010).

11. T. Chen, A. M. Chodara, A. J. Sprecher, F. Fang, W. Song, C. Tao, and J. J. Jiang, "A new method of reconstructing the human laryngeal architecture using micro-MRI," *J. Voice* **26**(5), 555-562 (2012) [doi: [10.1016/j.jvoice.2011.03.012](https://doi.org/10.1016/j.jvoice.2011.03.012)].
12. S. Schuberth, U. Hoppe, M. Döllinger, J. Lohscheller, and U. Eysholdt, "High-Precision Measurement of the Vocal Fold Length and Vibratory Amplitudes," *Laryngoscope* **112**(6), 1043-1049 (2002) [doi: [10.1097/00005537-200206000-00020](https://doi.org/10.1097/00005537-200206000-00020)].
13. N. A. George, F. F. de Mul, Q. Qiu, G. Rakhorst, and H. K. Schutte, "Depth-kymography: highspeed calibrated 3D imaging of human vocal fold vibration dynamics," *Phys. Med. Biol.* **53**(10), 2667-2675 (2008) [doi:[10.1088/0031-9155/53/10/015](https://doi.org/10.1088/0031-9155/53/10/015)].
14. L. Yu, G. Liu, M. Rubinstein, A. Saidi, B. J. F. Wong, and Z. Chen, "Office-based dynamic imaging of vocal cords in awake patients with swept-source optical coherence tomography," *J. Biomed. Opt.* **14**(6), 064020 (2009) [doi: [10.1117/1.3268442](https://doi.org/10.1117/1.3268442)].
15. C. A. Coughlan, L. Chou, J. C. Jing, J. J. Chen, S. Rangarajan, T. H. Chang, G. K. Sharma, K. Cho, D. Lee, J. A. Goddard, Z. Chen, and B. J. F. Wong, "In vivo cross-sectional imaging of the phonating larynx using long-range Doppler optical coherence tomography," *Sci. Rep-UK.* **6**, 22792 (2016) [doi: [10.1038/srep22792](https://doi.org/10.1038/srep22792)].
16. A. Lumsdaine and T. Georgiev, "Full resolution light field rendering," Technical Report (Indiana University and Adobe Systems, 2008).
17. E. Y. Lam, "Computational photography with plenoptic camera and light field capture: tutorial," *J. Opt. Soc. Am. A* **32**(11), 2021-2032 (2015) [doi: [10.1364/JOSAA.32.002021](https://doi.org/10.1364/JOSAA.32.002021)].
18. G. Lippmann, "Epreuves reversibles, photographies integrales," *J. Academic des sciences*, **146**(3), 446-451 (1908) [doi: [10.1051/jphystap:019080070082100](https://doi.org/10.1051/jphystap:019080070082100)].
19. N. Bedard, T. Shope, A. Hoberman, M. A. Haralam, N. Shaikh, J. Kovacevic, N. Balram, and I. Tomic, "Light field otoscope design for 3D in vivo imaging of the middle ear," *Bio. Opt. Exp.* **8**(1), 260-272, (2017) [doi: [10.1364/BOE.8.000260](https://doi.org/10.1364/BOE.8.000260)].

20. A. Hassanfiroozi, Y. Huang, B. Javidi, and H. D. Shieh, "Hexagonal liquid crystal lens array for 3D endoscopy," *Opt. Exp.* **23**(2), 971-981, (2015) [doi: [10.1364/OE.23.000971](https://doi.org/10.1364/OE.23.000971)].
21. M. Turola and S. Gruppeta, "4D Light Field Ophthalmoscope: a Study of Plenoptic Imaging of the Human Retina," *Frontiers in Optics, Optical Society of America*, paper JW3A.36, Orlando, United States, (2013) [doi: [10.1364/FIO.2013.JW3A.36](https://doi.org/10.1364/FIO.2013.JW3A.36)].
22. R. Prevedel, Y. Yoon, M. Hoffmann, N. Pak, G. Wetzstein, S. Kato, T. Schrödel, R. Raskar, M. Zimmer, E. Boyden, and A. Vaziri, "Simultaneous whole-animal 3D imaging of neuronal activity using light-field microscopy," *Nat. Methods* **11**(7), 727-730 (2014) [doi: [10.1038/nmeth.2964](https://doi.org/10.1038/nmeth.2964)].
23. V. Boominathan, K. Mitra, and A. Veeraraghavan, "Improving resolution and depth-of-field of light field cameras using a hybrid imaging system," *IEEE International Conference on Computational Photography*, Santa Clara, United States, 2-4 May 2014, (IEEE, 2014), pp. 1–10 [doi: [10.1109/ICCPHOT.2014.6831814](https://doi.org/10.1109/ICCPHOT.2014.6831814)].
24. See <http://lightfield.stanford.edu/lfs.html> for "The (New) Stanford Light Field Archive" (last accessed November 28, 2017).
25. C. Perwass and L. Wietzke, "Single Lens 3D-Camera with Extended Depth-of-Field," *Human Vision and Electronic Imaging XVII*, B. E. Rogowitz, T. N. Pappas and H. de Ridder, Ed., *Proc. SPIE* **8291**, Burlingame, United States, (2012) [doi: [10.1117/12.909882](https://doi.org/10.1117/12.909882)].
26. L. Gao, N. Bedard, and I. Tomic, "Disparity-to-depth calibration in light field imaging," *Computational Optical Sensing and Imaging 2016, Optical Society of America*, paper CW3D.2, Heidelberg, Germany, (2016) [doi: [10.1364/COSI.2016.CW3D.2](https://doi.org/10.1364/COSI.2016.CW3D.2)].
27. A. Ashok and M. A. Neifeld, "Compressive light field imaging," *Three-Dimensional Imaging, Visualization, and Display 2010 and Display Technologies and Applications for Defense, Security, and Avionics IV*, B. Javidi, J. Son, J. T. Thomas and D. D. Desjardins, Ed., *Proc. SPIE* **7690**, 76900Q, Orlando, United States (2010) [doi: [10.1117/2.1201008.003113](https://doi.org/10.1117/2.1201008.003113)].

28. S. D. Babacan, R. Ansorge, M. Luessi, P. R. Mataran, R. Molina, and A. K. Katsaggelos, "Compressive light field sensing," *IEEE Trans. Image Process.* **21**(12), 4746–4757, (2012) [doi: 10.1109/TIP.2012.2210237].
29. K. Marwah, G. Wetzstein, Y. Bando, and R. Raskar, "Compressive light field photography using overcomplete dictionaries and optimized projections," *ACM Trans. Graph.* **32**(4), 46 (2013) [doi: 10.1145/2342896.2342959].
30. S. Zhu, A. Lai, K. Eaton, P. Jin, and L. Gao, "On the fundamental comparison between unfocused and focused light field cameras," *Appl. Opt.* **57**(1), A1-A11 (2018) [doi: [10.1364/AO.57.0000A1](https://doi.org/10.1364/AO.57.0000A1)].
31. E. Hecht, *Optics*, Addison-Wesley, Boston, (1998) p. 424.
32. K. Siva, R. Krishna, and A. Aharma, "Chromatic aberrations of radial gradient-index lenses. I. Theory," *Appl. Opt.* **35**(7), 1032-1036 (1996) [doi: [10.1364/AO.35.001032](https://doi.org/10.1364/AO.35.001032)].
33. See <https://photron.com/mini-wx/> for Fastcam mini WX (Photron) (last accessed November 28, 2017).

Biographies and photographs for the other authors are not available.

Caption List

Fig. 1 Schematic of a light-field laryngoscope. (a) Optical setup. The detector arrays in the HR and LF channel are referred to as HR and LF detector array, respectively. (b) Photograph of the distal end of the probe.

Fig. 2 Flowchart of the image processing pipeline.

Fig. 3 Light-field reconstruction. (a) Image formation in one dimension. (b) Zoomed-in view of elemental images M_1 , M_2 , and M_3 . The disparity D is calculated as the relative distance between two matched image pixels. (c) Two-dimensional image reconstruction.

Fig. 4 Quantification of depth precision in light-field laryngoscope.

Fig. 5 Spatial resolution of the light-field laryngoscope. (a) Reconstructed in-focus image of a 1951 USAF resolution target. (b) Intensity profile along the green dashed line in Fig. 5(a) inset.

Fig. 6 3D phantom imaging. (a) Reference photograph of a tilted paper surface with letters. (b) Reconstructed 3D image. (c) Reference photograph of a vocal fold phantom. (d) Reconstructed 3D image.

Table 1 Specifications of two channels.